Ion-regulating Hybrid Electrolyte Interface for Long-life and Low N/P Ratio Lithium Metal Batteries

Ion-regulating Hybrid Electrolyte Interface for Long-life and Low N/P Ratio Lithium Metal Batteries

Abstract

Practical lithium metal batteries (LMBs) require full and reversible utilization of limited metallic Li anodes at a solid/quasi-solid electrolyte condition. This puts forward to a fundamental challenging issue on how to create compatible interphases to regulate interfacial ionic transport and protect the reactive metal. Herein, to address these issues, a robust cellulose-based composite gel electrolyte (r-CCE) capable of stabilizing ion deposition is reported via compositing bacterial cellulose (BC) skeleton with $Li_{6.4}La_3Zr_{1.4}Ta_{0.6}O_{12}$ (LLZTO) particles. Benefiting from the decoupled segment structure of cellulose and additional ionic channels of LLZTO, r-CCE not only achieves high ionic conductivity (1.68×10^{-3} S/cm) with a remarkable Li-ion transfer number (~0.92) and a wide window of electrochemical stability (~5.3 V), but also helps stabilize the Li anode. Utilizing ultrathin lithium metal anodes (15 μm), ultra-stable symmetric Li/Li cells that are armed with r-CCE demonstrate a highly stable plating/stripping process. Furthermore, a high areal capacity of ~4.2 mAh/cm^2, and 100 cycles with obviously improved stability of the full Li metal batteries with n/p ratio of ~0.74 is achieved.

Keywords: bacterial cellulose, lithium dendrite, composite gel electrolyte, lithium metal battery.

1. Introduction

Lithium (Li) metal anodes are considered as one of the most promising candidates for next-generation high-energy density rechargeable batteries, due to their high theoretical capacity (3860 mA/g, ~10 times higher than graphite anodes), low density (0.59 g/cm^3), and low reduction potential (-3.04 V *vs.* the standard hydrogen electrodes) [1, 2]. However, the large-scale practical application of Li anodes is restricted by their electro–chemo–mechanical instability during the repeated deposition/stripping processes [3-5]. Especially, the continuous breakdown/reconstruction of solid electrolyte interphase (SEI) layers leads to the excessive consumption of electrolyte and pulverization of Li anodes [6, 7]. More severely, the self-accelerated growth of Li dendrites penetrates the SEI layer and separators, resulting in sudden short-circuit and thereof thermal runaway [8, 9].

The issue of the uncontrollable growth of Li dendrites is often accompanied by the transport of Li ions and electrons as well as the chemical and electrochemical reactions at the anode-electrolyte interphase [10]. So far, tremendous efforts have been made to address the Li dendrite issue such as adopting well-designed conductive hosts, applying concentrated electrolytes [11, 12], electrolyte additives [13, 14], external pressure [15, 16], artificial protective layers at the electrode-electrolyte interfaces [17-19], modified separators [20-22], and quasi-/solid electrolyte [23-25]. Among these strategies, solid electrolyte is considered as the ultimate choice for next-generation lithium metal batteries because it can eliminate the safety hazards resulting from leakage or explosion of organic liquid electrolytes [26, 27]. Additionally, the desirable mechanical modulus of solid electrolyte is also expected to alleviate the growth of dendrite [28]. However, the solid electrolyte is still plagued by poor ionic conductivity and significantly increased interfacial resistance as compared with liquid electrolyte. As the promising alternative of solid electrolyte for practical applications, gel electrolytes (GEs) integrate the merits of high ionic conductivity and low interfacial resistance comparable to liquid electrolyte. Thus far, several GEs have been reported based on poly (vinylidene fluoride-co-hexafluoropropylene), polyurethane, polyacrylonitrile, poly (ethylene oxide), soybean protein, and cellulose, which have possessed improved ionic conductivity close to liquid electrolytes (1 mS/cm). However, the mechanical modulus of GEs is limited at the mega-pascal order due to their swollen polymeric nature, which is much lower than that of solid electrolyte and fails to meet the needs of dendrite suppression (> 1 GPa).

In addition to constructing a physical barrier, increasing the Li^+ transferring efficiency or stabilizing interfacial electrical field via restriction of anion diffusion can retard the nucleation of dendrite growth. Among these GE polymetric matrices (such as poly (ethylene oxide) [29], poly (vinylidene fluoride-hexafluoro propylene) [30], polyvinylidene fluoride [31]), cellulose and their derivates stand out owing to their promising properties such as high mechanical strength, good thermal stability, and abundant polar chemical groups (e.g., -OH, -O-, etc.) in cellulose chains [32]. These functionalities can further immobilize anion groups and aid in Li ion movement [33, 34]. Different from regular celluloses, which are obtained by fibrillation of fibers, bacterial cellulose is synthesized by bacteria named acetobacter [35]. Compared with other types of cellulose, bacterial cellulose exhibits higher molecular weight, higher purity, and higher crystallinity [36]. In particular, bacterial cellulose presents higher Young's modulus (10-35 GPa) than most of the other cellulose materials. However, cellulose polymetric matrix usually possesses higher crystallinity than other GE polymers, resulting in relatively lower solvation because of limited segment motion and narrow space between chains for solvated Li ions. Accordingly, the Li-ion transference number of cellulose-based GEs is usually limited below 0.5. Although numerous approaches have been investigated to further improve the Li-ion transference number including chemical modification of cellulose matrix by cross-link polymer, block polymer, single-ion conducting polymer, and introducing inorganic fillers, the Li-ion transference number of cellulose-based GEs barely approaches the level of inorganic single-ion solid electrolytes (e.g., LLTO, LLZTO, LATP, etc.). More importantly, similar to the polyethylene oxide, uncoordinated ether oxygens in cellulose generate the side reactions with solvents and Li salts under high voltage [37, 38], leading to the rapid capacity decay or even sudden failure. This drawback determines that cellulose-based GEs can only couple with low-voltage cathodes (e.g., $LiFePO_4$), instead of high-voltage cathode (e.g., Ni-rich/Li-rich cathodes), which fails to meet the urgent requirement of high energy density in practical energy storage systems. Therefore, more critical efforts on tradeoff between mechanical strength, Li-ion transference number, and electrochemical compatibility of cellulose-based GEs should be made.

Herein, we report a robust cellulose-based composite gel electrolyte (r-CCE) capable of tuning ion transport and stabilizing Li-ion deposition on Li metal anode. The r-CCE with excellent electrolyte wettability and mechanical/thermal durability is achieved via the construction of a unique nacre-like structure via calendering bacterial cellulose (BC) and $Li_{6.4}La_3Zr_{1.4}Ta_{0.6}O_{12}$ (LLZTO) particles. Besides, r-CCE simultaneously exhibits remarkable electrochemical

properties, including ionic conductivity, Li-ion transfer number (~0.92), and electrochemical window (~5.3 V) as well as stability. As a result, long-lived symmetric Li/Li cells with r-CCE at 0.5 mA/cm^2 for 870 h and at high current rates are demonstrated. Furthermore, the assembled Li/LiNi$_{8.15}$Co$_{1.5}$Al$_{0.35}$O$_2$ (NCA) cells with r-CCE present remarkably improved capacity (~4.48 mAh/cm^2), rate, and cyclic stability even with a high areal density of cathode materials (25 mg/cm^2) and limited lithium metal anode under a lean electrolyte condition.

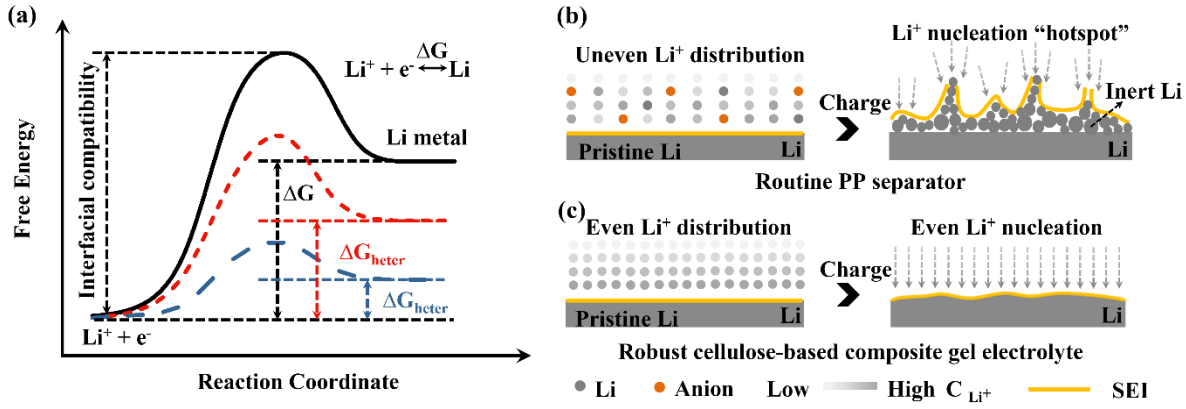

Figure 1. (a) Gibbs free energy change with lithophilic nucleation site. Schematic illustration of the electrochemical deposition behaviors of the Li metal anodes using (b) a commonly employed polypropylene (PP) separator and (c) a robust cellulose-based composite gel electrolyte (r-CCE) with the LLZTO as an ion redistributor with uniform Li-ion distribution properties.

3. Results and discussion

As illustrated in **Figure 1a**, the lithium nucleation process on the surface of Li metal anode can be explained by the change of Gibbs free energy. The homogeneous nucleation can be described as follows [39, 40]:

$$\Delta G_{homo} = -4/3\ \pi r^3 \Delta G_V + 4\ \pi r^2 \gamma \quad (1)$$

where the ΔG_{homo} and ΔG_V are the changes of Gibbs energy and volume Gibbs energy during homogeneous nucleation, respectively. r is the radius of nucleus and γ is the interfacial energy between liquid electrolyte and solid nucleus. As nucleation agents emerge, the nuclei tend to generate on the surface of the heterogenous surface. The change of Gibbs energy is related to the interfacial compatibility between nucleus and heterogeneous agents [41]. Optimization on interfacial compatibility is expected to guide the lithium nucleation process to suppress the growth of dendrites. Besides, the uniform concentration of lithium ions on the surface of Li

anode is another important factor for the stable lithium nucleation process. For the cells with routine PP separators in **Figure 1b**, the distribution of Li ions on the surface of Li metal anode are relatively uneven. Li ions are usually accumulated around the pores of separators, accordingly leading to low transfer efficiency of Li ions. But anions and solvated Li ions are simultaneously migrated on the surface of Li metal anode, resulting in the severe polarization and acceleration on growth of Li dendrites. In contrast, r-CCE can achieve excellent transport of Li ions and immobilization of anions, which simultaneously realizes the high-throughput and uniform Li ion distribution (**Figure 1c**). Hence, benefiting from the even and stable Li-ion field as well as interfacial engineering of nucleation process, the growth of Li dendrites is expected to be suppressed from the root.

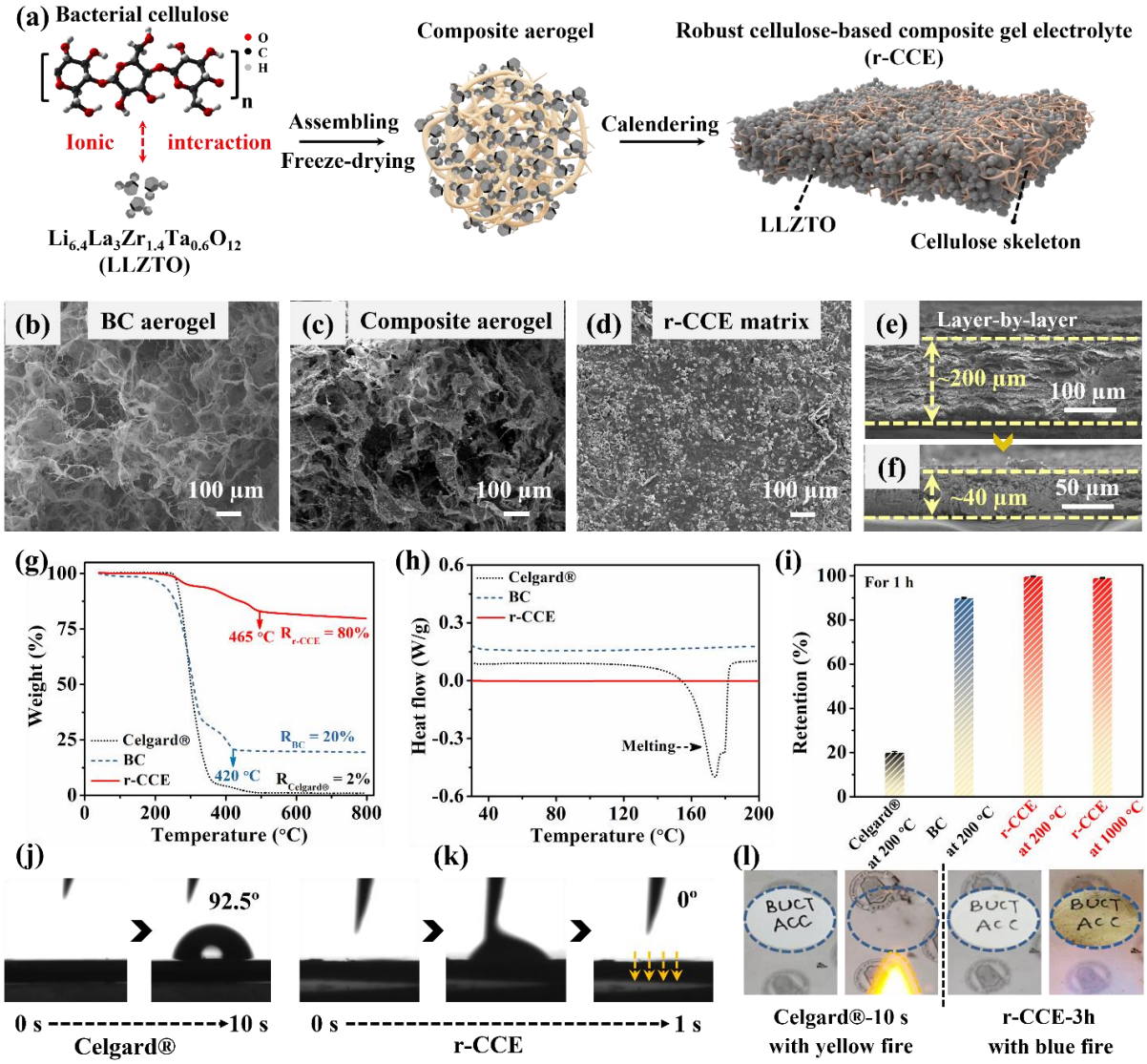

Figure 2. Unique nanoarchitecture and corresponding thermal stability as well as electrolyte wettability. (a) Schematic illustration of the fabrication of multifunctional r-CCE matrix. SEM images of (b) BC aerogel, (c) hybrid aerogel, (d) top view and (e) cross section

of r-CCE matrix before and (f) after calendaring. (g) Thermogravimetric curves of r-CCE matrix, BC and Celgard® separator. (h) Differential scanning calorimetry curve of r-CCE matrix, BC and Celgard® separator. (i) Shape retention of r-CCE matrix, BC and Celgard® separator at 200 and 1000 °C for 1 h. Surface contact angles of (j) Celgard® separator and (k) r-CCE matrix with 1 M $LiPF_6$/Ethylene carbonate (EC):dimethyl carbonate (DMC) (1:1 vol %). (l) Flame retardant performance of Celgard® separator and r-CCE matrix.

Construction of designable nanostructures is vital for electrolyte adsorption and mechanical performance in separators. The schematic illustration of the fabrication of r-CCE matrix is demonstrated in **Figure 2a**. Cellulose nanofibers are composed of various cellulose chains with abundant polar surface groups such as -OH and -C-O-, which forms strong hydrogen bonds with each other [42, 43]. Driven by abundant surface polar groups (*e.g.,* -OH, -O-) and physical entangling, BC nanofibers can self-assemble into interconnected nanofibrous structure and then be converted into aerogels via freeze-drying in **Figure 2b** [44, 45]. Furthermore, the magnified partial structure in **Figure S1** demonstrates that each wall in aerogel is constructed by amounts of physically tangled BC nanofibers. Inspired by the assembling process of BC nanofibers, LLZTO particles are introduced into assembling process of BC nanofibers to construct composite aerogel. Even with introduction of LLZTO particles, the composite aerogel still displays a hierarchical porous structure in **Figure 2c**. As displayed in **Figure S2a** and **b**, LLZTO particles are entangled by BC nanofibers on the wall of aerogels. After continuous calendering, the initial porous composite aerogels are compressed into dense composite membrane. LLZTO particles are well embedded into the BC skeleton in **Figure 2d** with numerous exposure LLZTO particles on the surface of membrane. The LLZTO particles with amorphous Li salt coating in r-CCE still possess good crystallinity in **Figure S3**. The emerging amorphous Li salt (*e.g.*, lithium carbonate, lithium hydroxide) on the LLZTO particles is attributed to the partial decomposition of LLZTO particles during the fabrication process. These lithium salts exhibit some solubility into the EC/DMC solvent of electrolyte, especially Li_2CO_3 according to the previous work and simulation [46-48]. With the increasing content of LLZTO, original nanofibrous BC structure with high crystallinity in **Figure S4** and **S5** gradually turns into an amorphous state due to the strong physical interaction and destructive effect on the ordered arrangement of polymer side chains [49], which is beneficial for the enhancement of ionic conductivity in the composites [50, 51]. The cross-sectional morphologies of r-CCE matrix before and after calenderization are shown in **Figure 2e, f**. The thickness of r-CCE matrix decreases from 200 to 40 μm, which meets the basic need for

preventing the short circuit and simultaneously shortening ion transport pathways. Additionally, the layer-by-layer structure of calendered r-CCE matrix is similar to the natural nacre structure in **Figure S6**, indicating the good mechanical strength and stiffness [52].

Thermal stability is a crucial property for separators to prevent thermal runaway and improve battery safety at the high-temperature condition. In contrast to the initial pyrolysis temperature of the Celgard® separator (263 °C), the BC separator displays a lower temperature of 248 °C. But with the introduction of the LLZTO fillers, r-CCE matrix exhibits a higher initial pyrolysis temperature (251 °C) in **Figure S7**. Furthermore, as shown in **Figure 2g**, the final solid content in r-CCE matrix reaches up to 80%, which is much higher than that of the BC (ca. 20%) and Celgard® separator (ca. 2%). In addition, the thermal stability of r-CCE matrix, BC, and Celgard® separator are further demonstrated by differential scanning calorimeter (DSC) measurements. As illustrated in **Figure 2h**, Celgard® separator shows the endothermic peak around 151 °C. However, r-CCE matrix and BC separator present no visible peak below 200 ºC, indicating a good thermal stability. Furthermore, the shrinkage retention of the Celgard®, BC, and r-CCE matrix after exposure at 200 °C for 1 h are shown in **Figure S8**. Specifically, the Celgard® and BC separators exhibit limited retention of 20% and 99%, respectively, which generates a potential risk of short circuits at high-temperature condition. In contrast, as shown in **Figure 2i**, r-CCE matrix after exposure at 200 ºC for 1 h still presents high retention of almost 100%. After exposure at 1000 ºC for 1 h or even 3 h, r-CCE matrix still displays the retention of 99%. Furthermore, the flame retardant performance of these separators is further investigated in **Figure 2l**. Celgard® separator burns into ash after only 10 s under the yellow fire flame (460 – 570 °C). Comparatively, r-CCE matrix displays the excellent flame retardant performance, which withstands the burning under high-temperature blue fire flame (>1150 °C) for 3 h. As compared with the reported works summarized in **Figure S9** [53-69], r-CCE matrix shows up to 3 times higher shape-stable temperature, indicating the huge potential for the safe energy storage systems at high-temperature condition.

Furthermore, the pore structure of r-CCE matrix is investigated by N_2-sorption isotherm analysis. As compared with sample accumulation of LLZTO particles, r-CCE matrix presents an isotherm curve with a hysteresis loop in **Figure S10a**, indicating the existence of mesopores. Benefiting from the nanofibrous structure of BC skeleton, the specific surface area of r-CCE matrix increases from 6 m^2/g to 20 m^2/g. In addition, the pore size distribution of r-CCE matrix calculated by the Barrett-Joyner-Halenda (BJH) model in **Figure S10b** displays a hierarchical

porous structure with dominant mesopores and macropores. It is known that hierarchical porous structure favors the infiltration and diffusion of liquid electrolyte for ionic conduction. The surface infiltration ability and wetting behavior of r-CCE matrix are further demonstrated via video optical angle measurements. As shown in Figure **2j** and **k**, Celgard® separator exhibits a limited wetting behavior for liquid electrolyte (1 M $LiPF_6$/EC:DMC, 1:1 vol%) with a large contacting angle of 92.5º even after 10 s. In contrast, the electrolyte droplet on the surface of r-CCE matrix penetrates it immediately within only 1 s. After immersion in liquid electrolyte in **Figure S11**, LLZTO particles still show the almost same crystal structure only with reducing exposure (211) crystal planes, demonstrating the good crystalline stability and compatibility with liquid electrolyte. Moreover, r-CCE matrix exhibits a higher porosity of 93±1% than that of BC separator (ca. 83±1%) and Celgard® separator (*ca.* 45±1%) in **Table S1**. Accordingly, r-CCE matrix presents the high electrolyte uptake of 392%, which is much higher than that of BC (*ca.* 320%) and Celgard® separator (*ca.* 200%), respectively. The excellent electrolyte infiltration and uptake behaviors are achieved by the synergetic effect between interconnected porous structure and abundant polar groups of BC nanofibers [70].

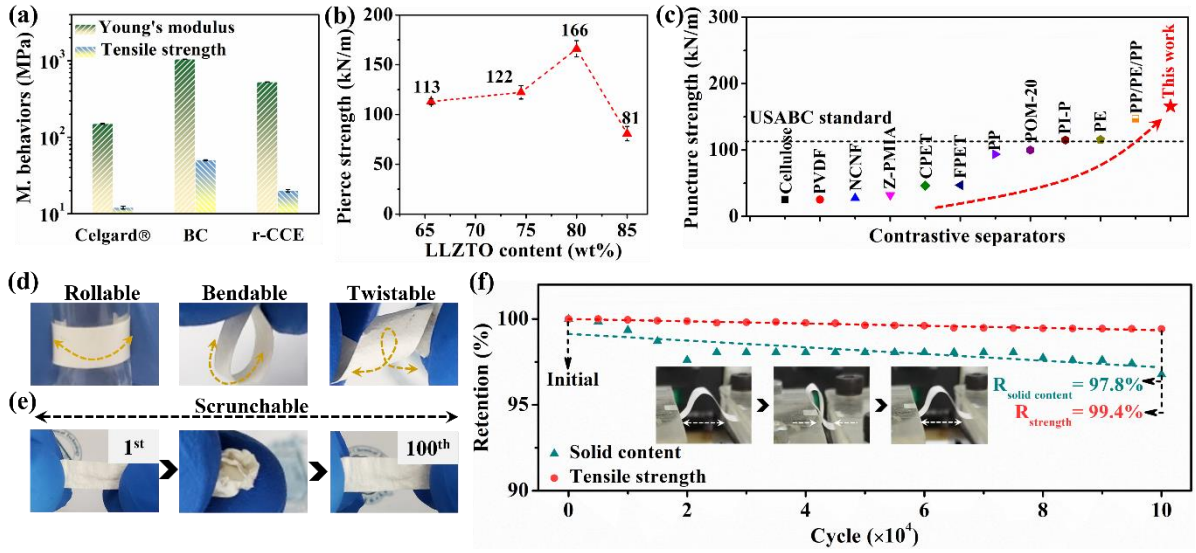

Figure 3. Mechanical properties of r-CCE as compared with its counterparts. (a) Tensile strength and Young's modulus of r-CCE, BC and Celgard® separator. (b) Pierce strength as a function of the LLZTO content. (c) Comparison of puncture strength of r-CCE with other reported separators (USABS: United States Advanced Battery Consortium). Photographs of r-CCE matrix (d) under different mechanical conditions and (e) lasting 100 times of scrunching process. (f) Long-term fatigue behaviors of r-CCE matrix with optical images of bending insert. (PVDF: polyvinylidene fluoride; NCNF: halloysite nanotube/polyvinylidene fluoride

nanocomposite nanofiber; Z-PMIA: ZIF-L/poly (m-phenylene isophthalamide); CPET: Al_2O_3-coated poly (ethylene terephthalate); FPET: Al_2O_3-filled poly (ethylene terephthalate); PP: polypropylene; PE: polyethylene; POM-20: polyformaldehyde/cellulose nanofibers; PI-P: polyimide nanofibers; PP/PE/PP: polypropylene/polyethylene/polypropylene) (Please see the references in Supporting Information).

Excellent mechanical behaviors are of critical importance for withstanding the strains from cell-assembly and blocking Li dendrites. As shown in **Figure S12**, with the infiltration of electrolyte, the tensile strength and Young's modulus decreases. But the tensile strength and Young's modulus of the BC separator and r-CCE are still notably higher than that of the Celgard® separator in **Figure 3a**. Specifically, the tensile strength of r-CCE is about 21 MPa, which is much higher than that of Celgard® separator (12 MPa). The cross-section images of r-CCE (**Figure S13**) show tight combination between the LLZTO particles and BC skeleton even withstanding severe tensile fractures. Besides, benefiting from the strong intermolecular interaction of the BC nanofibers (*e.g.,* van der Waals force and hydrogen bonding), r-CCE displays a high Young's modulus (527 MPa) in contrast with the PP separator (154 MPa).

Additionally, the pierce strength is an important parameter to evaluate the separators in practical applications. The increasing content of LLZTO is highly beneficial for the enhancement of pierce strength in **Figure 3b**. When reaching up to 80%, r-CCE shows a relatively higher pierce strength of 166 kN/m. As compared with other reported polymetric separators, r-CCE exhibits a better behavior with the highest puncture strength as shown in **Figure 3c** (Please see the references in Supporting Information). Moreover, even loaded with high LLZTO particles, r-CCE in **Figure 3d** displays the excellent flexibility, which can sustain various mechanical deformation such as rolling, twisting, folding, and even scrunch for 100 times without breaking down in **Figure 3e.** Moreover, lasting cyclic bending for 100,000 times in **Figure 3f**, r-CCE remains tensile strength of 99.4% and solid content of 97.8%. The surface morphologies of r-CCE lasting 100,000 times bending exhibits no obvious cracks in **Figure S14**. Furthermore, the thickness of the central section of r-CCE after long-term bending slightly increases in **Figure S15a**. But according to the magnified image in **Figure S15b**, LLZTO particles are still tightly embedded by BC nanofibrous skeleton. The excellent mechanical durability of the separator withstands the mechanical deformation and high tension during assembling, and prevents the internal short circuits owing to the debris of the rough electrodes [71].

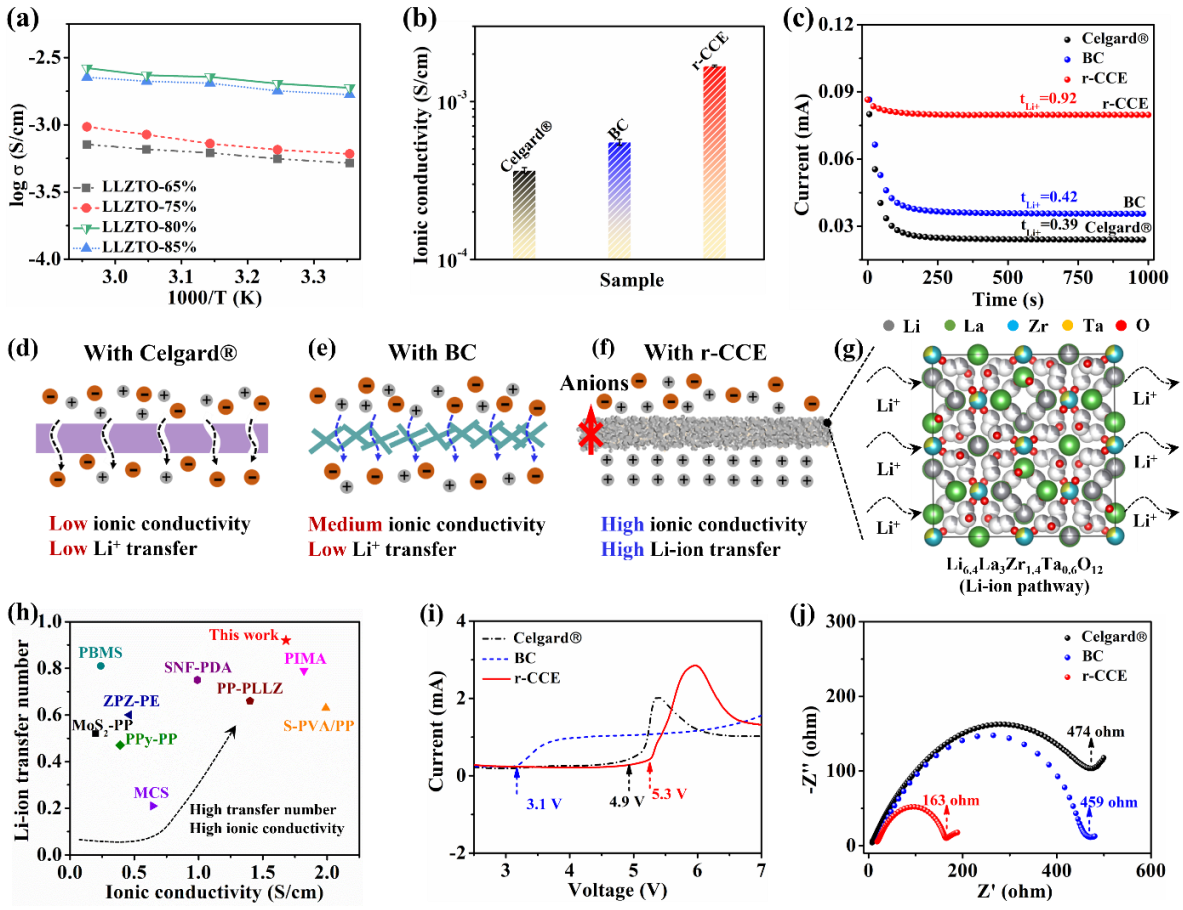

Figure 4. Electrochemical behaviors of r-CCE (with LLZTO weight ratio of 80%) as compared with its counterparts. (a) Ionic conductivity of r-CCE with different contents of LLZTO. (b) Comparison of ionic conductivity. (c) The chronoamperometric plots of the SS/separator/Li cells. (d) – (g) Schematic illustrations of ionic conduction in each separator. (h) Comparison of Li-ion transfer number as a function of ionic conductivity with other reported work. (i) Linear sweep voltammetry plots of Li/separator/SS cells at a scan rate of 10 mV/s. (j) Nyquist plots of Li/separator/Li cells. (MCS: Multilayer-coated separator; MoS_2-PP: MoS_2/polypropylene separator; PBMS: Prussian blue based Janus separator; S-PVA/PP: Silk fibroin/polyvinyl alcohol/polypropylene separator; PIMA: MOFs modified poly(m-phenylene isophthalamide) separator; PPy-PP: polypyrrole/ polypropylene separator; ZPZ-PE: Zirconia/POSS polyethylene separator; SNF-PDA: Silicone nanofilaments/polydopamine polyethylene separator; PP-PLLZ: Polypropylene/polyvinylidene fluoride/$Li_{6.4}La_3Zr_{1.4}Ta_{0.6}O_{12}$ separator) (Please see the references in Supporting Information).

The ionic conduction behaviors of separators are vital for the Li-ion conduction and distribution in LMBs. As illustrated in **Figure 4a**, with introduction of LLZTO, the ionic conductivity of

the separators gradually increases. And with the weight ratio of 80%, composite separator exhibits the highest conductivity. The ionic conductivity of r-CCE is shown in **Figure 4b** as compared with the counterparts. The r-CCE presents the ionic conductivity of 1.68×10^{-3} S/cm, which is up to 3 times higher than that of the BC separator (0.52×10^{-3} S/cm) and Celgard® separator (0.36×10^{-3} S/cm). Additionally, according to the calculation of impedance results in **Table S2**, r-CCE presents a Li-ion transfer number of 0.92 in **Figure 4c**, which is much higher than that in the case of the BC separator (0.42) and Celgard® separator (0.39).

As illustrated in **Figure 4d**, Celgard® separator with a comparatively low porosity of ca. 45% (see **Table S1**) results in a much higher resistance for ion-transport and low ionic conductivity. For BC separator in **Figure 4e**, the higher porosity (*ca.* 83%) and electrolyte uptake benefit the penetration of electrolytes and thereof reducing the ion-transport resistance. Meanwhile, the cellulose chains have interaction with Li ions by polar groups and capture the electrolyte solvent molecules (*i.e.,* EC), resulting in suppression of migration of PF_6^- anions and improved Li-ion transference number (0.43) [72, 73]. For further improvement in **Figure 4f**, as a Lewis base, amounts of LLZTO particles in r-CCE can greatly promote the Li-salt dissociation via strong binding with Li ions, which helps Li ion transport. Secondly, as the fast Li-ion conductors in **Figure 4g**, LLZTO particles provide another high-throughput pathway for Li-ion conduction, which can increase the overall Li-ion transference number and benefit the homogenization of Li ion and stabilization of Li deposition around interface. As compared with other reported separators summarized in **Figure 4h**, r-CCE integrates the higher ionic conductivity and Li-ion transfer number (Please see the references in Supporting Information).

In addition, it is found that electrochemical stability is remarkably improved by the introduction of LLZTO particles. As displayed in **Figure 4i**, a current peak around 4.9 V appears in the Celgard® separator, reflecting the decomposition of liquid electrolytes [74]. However, oxidative degradation of BC separators is found at 3.1 V, which is caused by the decomposition of components (*e.g.,* $LiPF_6$) in electrolyte. The decomposition reactions are attributed to the side effects between bound water trapped by the active hydroxyl groups in BC and electrolytes under a high electric field [37, 75]. Interestingly, r-CCE exhibits enhanced electrochemical stability with a wide potential range of 5.3 V due to the stable interphase contrasted by LLZTO particles. The introduction of numerous LLZTO particles can consume the extra bound water in the cellulose chains to reduce the side reaction of water molecules with $LiPF_6$ under high voltage. Meanwhile, the active ether oxygen and hydroxyl are easily coupled with Li ions of

LLZTO via the Lewis acid-base effect to avoid the oxidation reaction with solvent and lithium salts to further stabilize the electrochemical interface [76]. Furthermore, the interfacial compatibility between the electrolytes and Li anodes is investigated in **Figure 4j**. Specifically, the initial interface impedance spectra exhibit semicircles in the high-frequency region, demonstrating the charge-transfer resistance (R_{ct}). The charge-transfer resistance of r-CCE is only 163 Ω, which is lower than that of the BC (~459 Ω) and Celgard® separator (~475 Ω). The lower resistance demonstrates a more stable and compatible interface between the Li anode and r-CCE in contrast to that of the BC and Celgard® separators. The excellent interface behavior is favorable for a lower and more stable voltage polarization of the resulting cells.

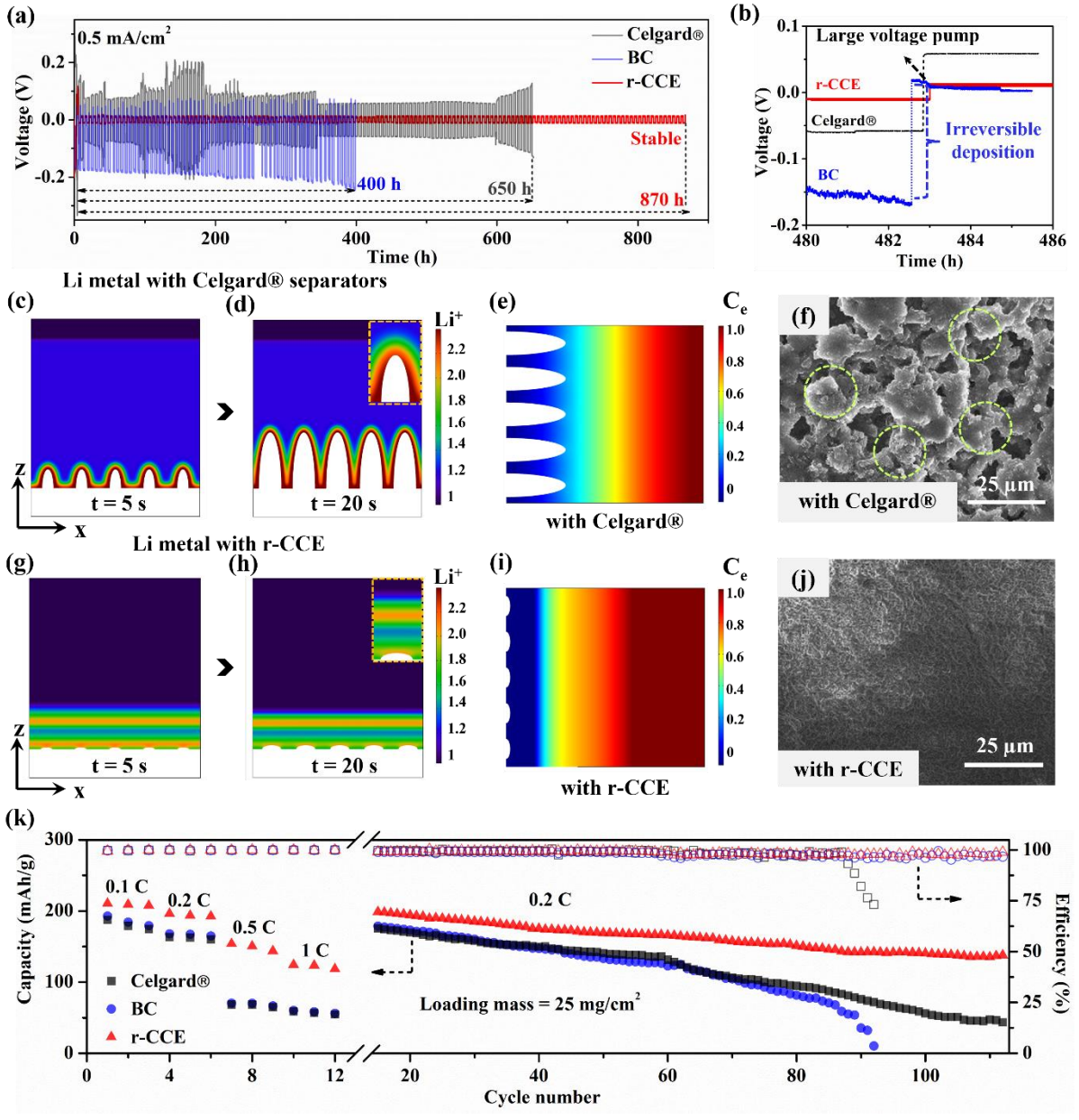

Figure 5. Li deposition behaviors and rate as well as cycling performance of

Li/separator/NCA cells. (a) Galvanostatic cycling curves of r-CCE, BC and Celgard® separator at 0.5 mA/cm^2. (b) Li stripping/plating voltage profiles in symmetric Li/Li cells with r-CCE, BC and Celgard® separator. Simulation of Li dendrite growth with (c, d) Celgard® separator and (g, h) r-CCE with Li-ion distribution on the surface of dendrites inset. Simulated concentration distribution of Li ions in electrolyte above Li anode with (e) Celgard® separator and (i) r-CCE. Surface morphologies of Li anode with (f) Celgard® separator and (j) r-CCE. (k) Rate and cycling performance of Li (15 μm)/NCA cells with r-CCE, BC and Celgard® separator.

The long-term electrochemical stability of r-CCE against Li metal is demonstrated using symmetric Li/Li cells in **Figure 5a**. The cell with Celgard® separator exhibits extremely high overpotential and unstable voltage profiles for 650 h at 0.5 mA/cm^2. The poor electrochemical behavior is inherently caused by the unstable Li deposition, which further induces severe Li dendrites growth on the surface of the Li anode. In contrast, the cell with r-CCE presents the lower polarization of ca. 3 mV with reversible voltage profiles for 870 h, demonstrating the highly reversible and stable Li plating/stripping process. The detailed galvanostatic charge/discharge curve of Celgard® in **Figure 5b** further reveals the existence of severe overpotential augmentation and high energy barrier. But the cell with r-CCE shows flat plateaus without an obvious "bump" during the charge/discharge process, demonstrating a lower energy barrier for both nucleation and stripping processes.

To further understand the effect of Li ion transportation and distribution on dendrite growth, the scenarios of dendrite growth with Celgard® separator and r-CCE are investigated by phase field method. According to the previous ionic conductivity and Li-ion transfer number (**see Figure 4b** and **c**), the Li dendrites grow severely on the surface of Li metal anode with Celgard® separator in **Figure 5c**. As shown in **Figure 5c inset**, the Li ions on the surface of Li metal anode are concentrated on the dendrites, which can further accelerate the growth of Li dendrites. As compared with that of Celgard® separator, the dendrite growth with r-CCE is suppressed in **Figure 5f**. And the Li ion distribution on the surface of Li metal anode is much more even than that of Celgard® separator (**Figure 5f inset**). Furthermore, in contrast to the electrolyte distribution with Celgard® separator in **Figure 5d**, the surface of Li metal anode with r-CCE exhibits the relatively low concentration of electrolyte due to the existence of LLZTO particles. The morphologies of the Li anodes after long-term cycling are shown in **Figure 5e** and **h.** As compared with the pristine Li anode in **Figure S16a**, the Li anode with

the Celgard® separator exhibits a highly rough surface in **Figure 5e**, indicating the severe Li dendrite growth caused by uncontrollable Li plating/stripping formation. The Li anode with the BC separator in **Figure S16b** exhibits a less rough and pointed surface because of mechanical suppression of the BC skeleton. In contrast, the Li anode with r-CCE displays the relatively smooth surface in **Figure 5h** due to the stable and even Li plating/stripping process. As shown in **Figure S17**, the cell with r-CCE is further tested at high current densities (*ca.* 1, 2, and 5 mA/cm^2). In particular, the cell still presents excellent cyclic stability with small overpotential and no visible voltage fluctuation even at 5 mA/cm^2. This excellent electrochemical stability is attributed to the high ionic conductivity and good interfacial compatibility, more significantly, the ability to stabilize the Li deposition.

As illustrated in **Figure 5i**, the electrochemical stability and compatibility of r-CCE are further examined by assembling LMBs. To meet the requirement of high-energy-density energy storage systems, $LiNi_{8.15}Co_{1.5}Al_{0.35}O_2$ with high working voltage and capacity is chosen as the cathode. More significantly, it is known that higher loading mass and designable N/P ratio as well as electrolyte content are more beneficial for the improvement of LMBs' practical energy density, but more challenging on resulting the rate and cycling performance. In this study, the loading mass of the cathode materials is about 25 mg/cm^2. The lithium metal anode and electrolyte content are also controlled with a N/P ratio of 0.74. Specifically, the cell with the Celgard® and BC separators in present the initial capacity of about 187 and 192 mAh/g at 0.1 C, respectively. Moreover, when the current density is raised to 1 C, the cells exhibit the capacity of 58 and 60 mAh/g (ca. 31% of capacity at 0.1 C). As a comparison, the cell with r-CCE displays a higher initial capacity of 210 mAh/g at 0.1 C. Even at a high current density of 1 C, r-CCE still presents a higher capacity of 124 mAh/g with a rate retention of 59%. The excellent rate performance of r-CCE cell implies that fast ion-transport kinetics can be achieved especially at high current rates owing to the decent Li-ion conductivity. According to the first charge/discharge curves **Figure S18**, the cell with r-CCE exhibits a higher Coulombic efficiency (*ca.* 89.3%) than that of cell with Celgard® separator (*ca.* 88.7%).

Furthermore, the cycling stability performances of assembled cells for 100 cycles at 0.2 C are shown in **Figure 5i**. The cell with Celgard® separator displays a severe capacity decay with the corresponding capacity retention of 25%. Especially for the cell with BC separator, the cell breakdown after 90 cycles. After 100 cycles, the cell with r-CCE presents relatively stable cycling performance as compared with the counterparts. The cell with r-CCE delivers a

reversible capacity of 138 mAh/g even after 100 cycles with a capacity retention of 70%. Moreover, the voltage profile of cell with r-CCE is shown in **Figure S19**. The cells with Celgard® and BC separators in **Figure S20a** and **b** show severe capacity decay due to the impedance buildup evidenced by the increasing polarization voltage. As compared with state-of-the-art lithium metal batteries with Li-ion transport engineering in **Table S3**, the cell with r-CCE exhibits the competitive capacity and stability. The improved electrochemical performance of the resulting batteries is attributed to the high-throughput Li ion transport and stable deposition process as well as excellent interfacial compatibility.

4. Conclusions

In summary, a robust cellulose-based composite gel electrolyte (r-CCE) capable of homogenizing Li ion distribution and stabilizing its deposition is reported. The r-CCE with nacre-like structure is fabricated by compositing bacterial cellulose skeleton and LLZTO particles via calendering. Benefiting from the unique hybrid structure, r-CCE exhibits high Young's and puncture modulus with excellent flexibility even lasting for 100,000 times bending fatigue test. Additionally, owing to the composite ceramic composition, r-CCE displays excellent thermal stability and flame retardant property. Meanwhile, as compared with other reported works, the resulting composite gel electrolyte simultaneously exhibit high ionic conductivity, Li-ion transfer number, and high stable voltage window. More significantly, the synergistic effect from robust BC skeleton and LLZTO NPs enabling lithium-ion deposition suppresses the growth of lithium dendrites effectively. Utilizing the ultrathin lithium metal anode (15 μm), ultra-stable symmetric Li/Li cells that is armed with r-CCE demonstrate a long cycle life of 870 hours at 0.5 mA/cm^2 and a highly stable plating/stripping process even at 5 mA/cm^2. Furthermore, a high areal capacity of ~4.2 mAh/cm^2, and 100 cycles with obviously improved stability of the full Li metal batteries with n/p ratio of ~0.74 is achieved. This study brings about a new insight on facile and practical creation of diverse range and types of separators to construct safe and reliable Li metal batteries, which could outperform conventional and advancing LMBs.

Data availability

The data that support the plots within this article and other findings of this study are available from the corresponding author upon reasonable request.

Acknowledgements

This work was supported by funding from the Energy Materials and Surface Sciences Unit of the Okinawa Institute of Science and Technology Graduate University, the OIST R&D Cluster Research Program, and the OIST Proof of Concept (POC) Program. We thank the OIST Micro/Nanofabrication Section and Imaging Section for the support. C.F.D. acknowledges the funding support by the Guangdong Basic and Applied Basic Research Foundation (Grant No. 2020A1515110830). Y.L. acknowledges the funding support by the Natural Science Foundation of Shandong Province (Grant No. ZR2020QE060). Y.H.Y. acknowledges the funding support by the National Natural Science Foundation of China (Grant No. 51772016). We also thank Prof. Wei-Hong Zhong and the Franceschi Microscopy & Imaging Center at Washington State University.

Author contributions

Y.B.Q. supervised the project. Y.B.Q. and C.F.D. conceived the idea and designed the experiments. C.F.D. fabricated the lithium metal batteries and performed experiments. Y.L., L.K.O., G.Q.T., C.Y.Z., J.H.Z., J.L.L., and Y.H.Y. provided valuable suggestions for the experiments. B.B.C. performed simulations for this study. All authors contributed to writing the paper.

Competing interests

The authors declare no competing interests.

References

[1] X.-B. Cheng, R. Zhang, C.-Z. Zhao, Q. Zhang, Chemical reviews, 117 (2017) 10403-10473.

[2] B. Liu, J.-G. Zhang, W. Xu, Joule, 2 (2018) 833-845.

[3] L. Li, S. Basu, Y. Wang, Z. Chen, P. Hundekar, B. Wang, J. Shi, Y. Shi, S. Narayanan, N. Koratkar, Science, 359 (2018) 1513-1516.

[4] J. Xiao, Science, 366 (2019) 426-427.

[5] G. Rong, X. Zhang, W. Zhao, Y. Qiu, M. Liu, F. Ye, Y. Xu, J. Chen, Y. Hou, W. Li, Advanced Materials, 29 (2017) 1606187.

[6] S. Xin, Y. You, S. Wang, H.-C. Gao, Y.-X. Yin, Y.-G. Guo, ACS Energy Letters, 2 (2017) 1385-1394.

[7] D. Wang, W. Zhang, W. Zheng, X. Cui, T. Rojo, Q. Zhang, Advanced Science, 4 (2017) 1600168.

[8] W. Luo, L. Zhou, K. Fu, Z. Yang, J. Wan, M. Manno, Y. Yao, H. Zhu, B. Yang, L. Hu, Nano letters, 15 (2015) 6149-6154.

[9] C. Fang, J. Li, M. Zhang, Y. Zhang, F. Yang, J.Z. Lee, M.-H. Lee, J. Alvarado, M.A. Schroeder, Y. Yang, Nature, 572 (2019) 511-515.

[10] C. Fang, B. Lu, G. Pawar, M. Zhang, D. Cheng, S. Chen, M. Ceja, J.-M. Doux, H. Musrock, M. Cai, Nature Energy, 6 (2021) 987-994.
[11] J. Qian, B.D. Adams, J. Zheng, W. Xu, W.A. Henderson, J. Wang, M.E. Bowden, S. Xu, J. Hu, J.G. Zhang, Advanced Functional Materials, 26 (2016) 7094-7102.
[12] X. Ren, S. Chen, H. Lee, D. Mei, M.H. Engelhard, S.D. Burton, W. Zhao, J. Zheng, Q. Li, M.S. Ding, Chem, 4 (2018) 1877-1892.
[13] J. Zheng, M.H. Engelhard, D. Mei, S. Jiao, B.J. Polzin, J.-G. Zhang, W. Xu, Nature Energy, 2 (2017) 1-8.
[14] Z. Chang, Y. Qiao, H. Yang, X. Cao, X. Zhu, P. He, H. Zhou, Angewandte Chemie International Edition, 60 (2021) 15572-15581.
[15] C. Niu, H. Lee, S. Chen, Q. Li, J. Du, W. Xu, J.-G. Zhang, M.S. Whittingham, J. Xiao, J. Liu, Nature Energy, 4 (2019) 551-559.
[16] A.J. Louli, M. Genovese, R. Weber, S. Hames, E. Logan, J. Dahn, Journal of The Electrochemical Society, 166 (2019) A1291.
[17] J. Zhao, L. Liao, F. Shi, T. Lei, G. Chen, A. Pei, J. Sun, K. Yan, G. Zhou, J. Xie, Journal of the American Chemical Society, 139 (2017) 11550-11558.
[18] G. Zheng, S.W. Lee, Z. Liang, H.-W. Lee, K. Yan, H. Yao, H. Wang, W. Li, S. Chu, Y. Cui, Nature Nanotechnology, 9 (2014) 618-623.
[19] Y. Xu, L. Gao, L. Shen, Q. Liu, Y. Zhu, Q. Liu, L. Li, X. Kong, Y. Lu, H.B. Wu, Matter, 3 (2020) 1685-1700.
[20] L. Tan, Y. Sun, C. Wei, Y. Tao, Y. Tian, Y. An, Y. Zhang, S. Xiong, J. Feng, Small, 17 (2021) 2007717.
[21] Z. Li, M. Peng, X. Zhou, K. Shin, S. Tunmee, X. Zhang, C. Xie, H. Saitoh, Y. Zheng, Z. Zhou, Advanced Materials, 33 (2021) 2100793.
[22] C.-Z. Zhao, P.-Y. Chen, R. Zhang, X. Chen, B.-Q. Li, X.-Q. Zhang, X.-B. Cheng, Q. Zhang, Science Advances, 4 (2018) eaat3446.
[23] T. Jiang, P. He, G. Wang, Y. Shen, C.W. Nan, L.Z. Fan, Advanced Energy Materials, 10 (2020) 1903376.
[24] D.H. Tan, A. Banerjee, Z. Chen, Y.S. Meng, Nature Nanotechnology, 15 (2020) 170-180.
[25] X. Wu, Y. Zheng, W. Li, Y. Liu, Y. Zhang, Y. Li, C. Li, Energy Storage Materials, 41 (2021) 436-447.
[26] X. Wu, K. Chen, Z. Yao, J. Hu, M. Huang, J. Meng, S. Ma, T. Wu, Y. Cui, C. Li, Journal of Power Sources, 501 (2021) 229946.
[27] J. Hu, K. Chen, Z. Yao, C. Li, Science Bulletin, 66 (2021) 694-707.
[28] J. Liu, H. Yuan, H. Liu, C.Z. Zhao, Y. Lu, X.B. Cheng, J.Q. Huang, Q. Zhang, Advanced Energy Materials, (2021) 2100748.
[29] H. Gao, Y. Huang, Z. Zhang, J. Huang, C. Li, Electrochimica Acta, 360 (2020) 137014.
[30] G. Chen, F. Zhang, Z. Zhou, J. Li, Y. Tang, Advanced Energy Materials, 8 (2018) 1801219.
[31] W. Ren, C. Ding, X. Fu, Y. Huang, Energy Storage Materials, 34 (2021) 515-535.
[32] Z. Wang, Y.H. Lee, S.W. Kim, J.Y. Seo, S.Y. Lee, L. Nyholm, Advanced Materials, 33 (2021) 2000892.
[33] L. Deng, Y. Wang, C. Cai, Z. Wei, Y. Fu, Carbohydrate Polymers, 274 (2021) 118620.
[34] Y. Li, Z. Sun, D. Liu, S. Lu, F. Li, G. Gao, M. Zhu, M. Li, Y. Zhang, H. Bu, Energy & Environmental Materials, 4 (2021) 434-443.
[35] A. Nakagaito, S. Iwamoto, H. Yano, Applied Physics A, 80 (2005) 93-97.
[36] R.J. Moon, A. Martini, J. Nairn, J. Simonsen, J. Youngblood, Chemical Society Reviews, 40 (2011) 3941-3994.
[37] J. Sheng, S. Tong, Z. He, R. Yang, Cellulose, 24 (2017) 4103-4122.
[38] F.J. Simon, M. Hanauer, F.H. Richter, J.r. Janek, ACS Applied Materials & Interfaces, 12 (2020) 11713-11723.
[39] D.R. Ely, R.E. García, Journal of the Electrochemical Society, 160 (2013) A662.
[40] D.R. Ely, A. Jana, R.E. García, Journal of Power Sources, 272 (2014) 581-594.

[41] Y. Liu, S. Xiong, J. Wang, X. Jiao, S. Li, C. Zhang, Z. Song, J. Song, Energy Storage Materials, 19 (2019) 24-30.
[42] M. Nogi, S. Iwamoto, A.N. Nakagaito, H. Yano, Advanced materials, 21 (2009) 1595-1598.
[43] M. Pääkkö, M. Ankerfors, H. Kosonen, A. Nykänen, S. Ahola, M. Österberg, J. Ruokolainen, J. Laine, P.T. Larsson, O. Ikkala, Biomacromolecules, 8 (2007) 1934-1941.
[44] C. Ding, L. Huang, X. Yan, F. Dunne, S. Hong, J. Lan, Y. Yu, W.H. Zhong, X. Yang, Advanced Functional Materials, 30 (2020) 1907486.
[45] C. Ding, X. Fu, H. Li, J. Yang, J.L. Lan, Y. Yu, W.H. Zhong, X. Yang, Advanced Functional Materials, 29 (2019) 1904547.
[46] W. Xia, B. Xu, H. Duan, X. Tang, Y. Guo, H. Kang, H. Li, H. Liu, Journal of the American Ceramic Society, 100 (2017) 2832-2839.
[47] K. Tasaki, A. Goldberg, J.-J. Lian, M. Walker, A. Timmons, S.J. Harris, Journal of The Electrochemical Society, 156 (2009) A1019.
[48] S. Klein, P. Harte, J. Henschel, P. Bärmann, K. Borzutzki, T. Beuse, S. van Wickeren, B. Heidrich, J. Kasnatscheew, S. Nowak, Advanced Energy Materials, 11 (2021) 2003756.
[49] L. Gao, B. Tang, H. Jiang, Z. Xie, J. Wei, Z. Zhou, Advanced Sustainable Systems, 6 (2022) 2100389.
[50] Y. Wang, A. Gozen, L. Chen, W.H. Zhong, Advanced Energy Materials, 7 (2017) 1601767.
[51] C. Yang, Q. Wu, W. Xie, X. Zhang, A. Brozena, J. Zheng, M.N. Garaga, B.H. Ko, Y. Mao, S. He, Y. Gao, P. Wang, M. Tyagi, F. Jiao, R. Briber, P. Albertus, C. Wang, S. Greenbaum, Y.-Y. Hu, A. Isogai, M. Winter, K. Xu, Y. Qi, L. Hu, Nature, 598 (2021) 590-596.
[52] F. De Luca, R. Menzel, J.J. Blaker, J. Birkbeck, A. Bismarck, M.S. Shaffer, ACS Applied Materials & Interfaces, 7 (2015) 26783-26791.
[53] Q. Song, A. Li, L. Shi, C. Qian, T.G. Feric, Y. Fu, H. Zhang, Z. Li, P. Wang, Z. Li, H. Zhai, X. Wang, M. Dontigny, K. Zaghib, A.-H. Park, K. Myers, X. Chuan, Y. Yang, Energy Storage Materials, 22 (2019) 48-56.
[54] R.R. Kohlmeyer, G.A. Horrocks, A.J. Blake, Z. Yu, B. Maruyama, H. Huang, M.F. Durstock, Nano Energy, 64 (2019).
[55] M.-T.F. Rodrigues, K. Kalaga, H. Gullapalli, G. Babu, A.L.M. Reddy, P.M. Ajayan, Advanced Energy Materials, 6 (2016).
[56] L. Ma, R. Chen, Y. Hu, W. Zhang, G. Zhu, P. Zhao, T. Chen, C. Wang, W. Yan, Y. Wang, L. Wang, Z. Tie, J. Liu, Z. Jin, Energy Storage Materials, 14 (2018) 258-266.
[57] L.L. Zuo, Q. Ma, S.C. Li, B.C. Lin, M. Fan, Q.H. Meng, X.W. Wu, Y.G. Guo, X.X. Zeng, Advanced Energy Materials, 11 (2020).
[58] Y. Han, L. Ye, B. Boateng, Q. Sun, C. Zhen, N. Chen, X. Shi, J.H. Dickerson, X. Li, W. He, Journal of Materials Chemistry A, 7 (2019) 1410-1417.
[59] Y. Yang, J. Zhang, Advanced Energy Materials, 8 (2018).
[60] X. Jiang, X. Zhu, X. Ai, H. Yang, Y. Cao, ACS Appl Mater Interfaces, 9 (2017) 25970-25975.
[61] H.-Y. Li, G.-A. Li, Y.-Y. Lee, H.-Y. Tuan, Y.-L. Liu, Energy Technology, 4 (2016) 551-557.
[62] K. Hwang, B. Kwon, H. Byun, Journal of Membrane Science, 378 (2011) 111-116.
[63] M. Waqas, C. Tan, W. Lv, S. Ali, B. Boateng, W. Chen, Z. Wei, C. Feng, J. Ahmed, J.B. Goodenough, W. He, ChemElectroChem, 5 (2018) 2722-2728.
[64] H. Gwon, K. Park, S.C. Chung, R.H. Kim, J.K. Kang, S.M. Ji, N.J. Kim, S. Lee, J.H. Ku, E.C. Do, S. Park, M. Kim, W.Y. Shim, H.S. Rhee, J.Y. Kim, J. Kim, T.Y. Kim, Y. Yamaguchi, R. Iwamuro, S. Saito, G. Kim, I.S. Jung, H. Park, C. Lee, S. Lee, W.S. Jeon, W.D. Jang, H.U. Kim, S.Y. Lee, D. Im, S.G. Doo, S.Y. Lee, H.C. Lee, J.H. Park, Proc Natl Acad Sci U S A, 116 (2019) 19288-19293.
[65] X. Jiang, L. Xiao, X. Ai, H. Yang, Y. Cao, Journal of Materials Chemistry A, 5 (2017) 23238-23242.

[66] J. Zhang, L. Yue, Q. Kong, Z. Liu, X. Zhou, C. Zhang, Q. Xu, B. Zhang, G. Ding, B. Qin, Y. Duan, Q. Wang, J. Yao, G. Cui, L. Chen, Sci Rep, 4 (2014) 3935.
[67] T.W. Zhang, B. Shen, H.B. Yao, T. Ma, L.L. Lu, F. Zhou, S.H. Yu, Nano Lett, 17 (2017) 4894-4901.
[68] H. Li, D. Wu, J. Wu, L.-Y. Dong, Y.-J. Zhu, X. Hu, Advanced Materials, 29 (2017) 1703548.
[69] J. Shi, Y. Xia, Z. Yuan, H. Hu, X. Li, H. Zhang, Z. Liu, Scientific Reports, 5 (2015) 8255.
[70] J. Li, Y. Cai, H. Wu, Z. Yu, X. Yan, Q. Zhang, T.Z. Gao, K. Liu, X. Jia, Z. Bao, Advanced Energy Materials, 11 (2021) 2003239.
[71] J. Zhang, L. Yue, Q. Kong, Z. Liu, X. Zhou, C. Zhang, Q. Xu, B. Zhang, G. Ding, B. Qin, Y. Duan, Q. Wang, J. Yao, G. Cui, L. Chen, Scientific Reports, 4 (2014) 3935.
[72] Q. Lu, Y.B. He, Q. Yu, B. Li, Y.V. Kaneti, Y. Yao, F. Kang, Q.H. Yang, Advanced Materials, 29 (2017) 1604460.
[73] Y. Wang, J. Qiu, J. Peng, J. Li, M. Zhai, Journal of Materials Chemistry A, 5 (2017) 12393-12399.
[74] M. Zhu, J. Wu, W.H. Zhong, J. Lan, G. Sui, X. Yang, Advanced Energy Materials, 8 (2018) 1702561.
[75] K. Tasaki, K. Kanda, S. Nakamura, M. Ue, Journal of The Electrochemical Society, 150 (2003) A1628-A1636.
[76] F. Huang, W. Liu, P. Li, J. Ning, Q. Wei, Materials, 9 (2016) 75.

The table of contents entry

Keywords: bacterial cellulose, lithium dendrite, composite gel electrolyte, lithium metal battery.

Title: Ion-regulating Hybrid Electrolyte Interface for Long-life and Low N/P Ratio Lithium Metal Batteries

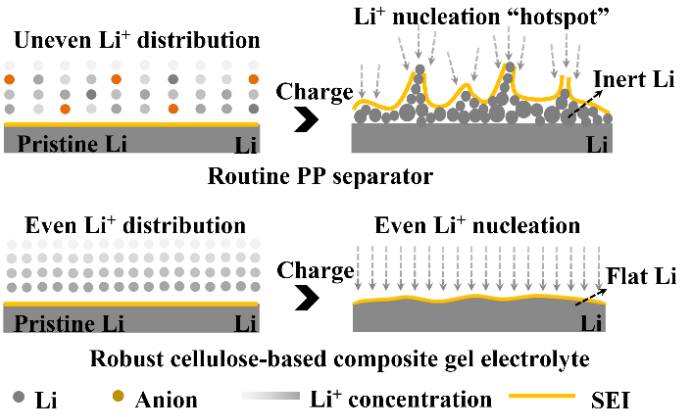

Highlights:

• A robust cellulose-based composite gel electrolyte (r-CCE) capable of stabilizing ion deposition is reported via compositing bacterial cellulose skeleton with $Li_{6.4}La_3Zr_{1.4}Ta_{0.6}O_{12}$ particles.

• r-CCE not only achieves high ionic conductivity (1.68×10^{-3} S/cm) with a remarkable Li-ion transfer number (~0.92) and a wide window of electrochemical stability (~5.3 V), but also helps stabilize the Li anode.

• Utilizing ultrathin lithium metal anodes (15 μm), ultra-stable symmetric Li/Li cells that are armed with r-CCE demonstrate a highly stable plating/stripping process.

• A high areal capacity of ~4.2 mAh/cm^2, and 100 cycles with obviously improved stability of the full Li metal batteries with n/p ratio of ~0.74 is achieved.